DOI: 10.1002/ ((please add manuscript number))

Article type: Full Paper

Title: High Efficiency Perovskite-Silicon Tandem Solar Cells: Effect of Surface Coating versus Bulk Incorporation of 2D Perovskite

The Duong, Huyen Pham, Teng Choon Kho, Pheng Phang, Kean Chern Fong, Di Yan, Yanting Yin, Jun Peng, Md Arafat Mahmud, Saba Gharibzadeh, Bahram Abdollahi Nejand, Ihteaz M. Hossain, Motiur Rahman Khan, Naeimeh Mozaffari, YiLiang Wu, Heping Shen, Jianghui Zheng, Haoxin Mai, Wensheng Liang, Chris Samundsett, Matthew Stocks, Keith McIntosh, Gunther G. Andersson, Uli Lemmer, Bryce S. Richards, Ulrich W. Paetzold, Anita Ho-Ballie, Yun Liu, Daniel Macdonald, Andrew Blakers, Jennifer Wong-Leung, Thomas White, Klaus Weber, Kylie Catchpole**

Dr. The Duong, Teng Choon Kho, Dr. Pheng Phang, Dr. Kean Chern Fong, Dr. Di Yan, Dr. Jun Peng, Dr. Md Arafat Mahmud, Naeimeh Mozaffari, Dr. YiLiang Wu, Dr. Heping Shen, Dr. Wensheng Liang, Chris Samundsett, Dr. Matthew Stocks, Prof. Daniel Macdonald, Prof. Andrew Blakers, Prof. Thomas White, Prof. Klaus Weber, Prof. Kylie Catchpole

Research School of Electrical, Energy and Materials Engineering, The Australian National University, Canberra 2601, Australia.
E-mail: the.duong@anu.edu.au, kylie.catchpole@anu.edu.au

Huyen Pham, Prof. Jennifer Wong-Leung
Department of Electronic Materials Engineering, Research School of Physics, The Australian National University, Canberra 2601, Australia.

Yanting Yin, Prof. Gunther G. Andersson

Flinders Institute for Nanoscale Science and Technology, Flinders University, Adelaide SA 5042, Australia.

Flinders Microscopy and Microanalysis, College of Science and Engineering, Flinders University, Adelaide, SA 5042, Australia

Saba Gharibzadeh, Dr. Bahram Abdollahi Nejand, Ihteaz M. Hossain, Dr. Motiur Rahman Khan, Prof. Uli Lemmer, Prof. Bryce S. Richards, Dr. Ulrich W. Paetzold

Institute of Microstructure Technology, Karlsruhe Institute of Technology, Hermann-von-Helmholtz-Platz 1, 76344 Eggenstein-Leopoldshafen Karlsruhe, Germany

Light Technology Institute, Karlsruhe Institute of Technology, Engesserstrasse 13, 76131 Karlsruhe, Germany

Dr. Jianghui Zheng, Prof. Anita Ho-Ballie

Australian Centre for Advanced Photovoltaics (ACAP), School of Photovoltaic and Renewable Energy Engineering, University of New South Wales, Sydney 2052, Australia.

Haoxin Mai, Prof. Yun Liu

Research School of Chemistry, The Australian National University, Canberra 2601, Australia

Dr. Keith McIntosh

PV Lighthouse, Coledale NSW 2515, Australia

Keywords: perovskite solar cell, wide bandgap, surface coating, perovskite-silicon tandem, 2-dimentional perovskite

Mixed-dimensional perovskite solar cells combining 3D and 2D perovskites have recently attracted wide interest owing to improved device efficiency and stability. Yet, it remains unclear which method of combining 3D and 2D perovskites works best to obtain a mixed-dimensional system with the advantages of both types. To address this, we investigated different strategies of combining 2D perovskites with a 3D perovskite, namely surface coating and bulk incorporation. We found that through surface coating with different aliphatic alkylammonium bulky cations, a Ruddlesden-Popper 'quasi-2D' perovskite phase was formed on the surface of the 3D perovskite which passivated the surface defects and significantly improved the device performance. In contrast, incorporating those bulky cations into the bulk induced the formation of the pure 2D perovskite phase throughout the bulk of the 3D perovskite, which negatively affected the crystallinity and electronic structure of the 3D perovskite framework and reduced the device performance. Using the surface coating strategy with n-butylammonium bromide to fabricate semi-transparent perovskite cells and combining with silicon cells in four-terminal tandem configuration, we achieved 27.7% tandem efficiency with interdigitated back-contact (IBC) silicon bottom cells (size-unmatched) and 26.2% with passivated emitter with rear locally-diffused (PERL) silicon bottom cells in a $1cm^2$ size-matched tandem.

1. Introduction

Perovskite cells have attracted tremendous interest in the photovoltaic community due to their high efficiency and potentially low fabrication cost. From the first reported efficiency of 3.8% in 2009[1], the efficiency of single junction perovskite solar cells has skyrocketed to 25.2% approaching the record of the currently dominating silicon technology[2]. Perovskite solar cells (PSCs) have the potential to not only compete with existing photovoltaic technologies, but to be combined with silicon solar cells in tandem configurations to target an efficiency of greater than 30%[3]. To date, efficiency of 28% has been achieved for perovskite-silicon tandem in a two-terminal configuration while an efficiency of 27.1% has been attained in a four-terminal configuration[4]. Further steps to improve the overall tandem efficiency involve enhancing the efficiency of each sub-cell, especially the perovskite top cells, and managing the light more efficiently[5]. In term of enhancing the efficiency of PSCs, there has been increasing interest in utilizing mixed-dimensional perovskites by combining 3D and 2D perovskites. 2D perovskites especially the ones arranged in Ruddlesden Popper phases are a class of quantum well-like materials with the general formula $R_2A_{n-1}B_nX_{3n+1}$. Here, n defines the number of inorganic sheets which are intercalated with bulky organic cations R acting as a spacer between the inorganic sheets and X is a halide anion[6]. Thus, when $n = 1$, a pure 2D perovskite R_2BX_4 is formed. By introducing a small organic cation A and increasing $n \geq 2$, a multi-layer 'quasi-2D' perovskite is formed and finally converges to the 3D perovskite as $n \rightarrow \infty$[7]. In a 2D perovskite, the atomic size constraints are significantly relaxed, compared to Goldschmidt tolerance factors that determine the formation of 3D perovskites[8]. This enables a wide range of choices for the bulky organic cations R to be designed and engineered, thus obtaining the desired optical and electronic properties[7]. In addition, various strategies can be applied to combine 2D perovskites with 3D perovskites with the aim of enhancing both device efficiency and stability. Wang et al. incorporated n-butylammonium cations into 3D mixed-cation mixed-halide perovskites $FA_{0.83}Cs_{0.17}Pb(I_{y}Br_{1-y})_3$ (where FA is formamidinium), which led to the formation of 2D perovskite platelets and suppressed the non-radiative charge recombination in the devices[9]. Other researchers added a small amount of phenylethylammonium (PEA) cations into the 3D perovskite precursor, which led to the formation of the 2D perovskite at grain boundaries and suppressed the ion migration[10]. Using a very different strategy, Koh *et al.* and Cho *et al.* used bulky organic cations n-butylammonium and/or iso-butylammonium to passivate the surface of the 3D perovskite which enhanced both the efficiency and moisture resistance of the devices[11]. Gharibzadeh et al. demonstrated a record open circuit voltage (V_{OC}) of up to 1.31 V using n-butylammonium bromide to passivate the surface of $FA_{0.83}Cs_{0.17}Pb(I_{0.6}Br_{0.4})_3$ perovskite[12]. Utilizing PEA cations, Cho *et al.* also used a surface coating approach and found that the selective growth of a pure 2D perovskite PEA_2PbI_4 layer on the surface of the 3D perovskite improved the charge transfer and reduced the charge recombination[13]. Overall, it can be observed that different strategies have been applied to combine 2D perovskite with the 3D perovskite, however it is unclear which strategy works the best for each combination of 2D and 3D perovskites. In this work, we explored two different strategies for combined 2D / 3D perovskites, namely: i) surface coating of the 2D perovskite onto a pre-existing 3D perovskite layer; and ii) mixing the precursors together such that the 2D perovskite was incorporated into the bulk of the 3D perovskite. With regard to the chosen materials, we focused on various aliphatic alkylammonium bulky cations such as n-butylammonium, iso-butylammonium and t-butylammonium (all known to form 2D structures) and a quadruple-cation mixed-halide 3D perovskite, exhibiting a bandgap of 1.72 eV that was optimized for tandem applications[14]. We found that the two 2D treatment strategies caused vastly different impacts on the crystallinity, optical properties and electronic structure of the mixed-dimensional perovskite, leading to contrasting trends in the device performance. Using X-ray diffraction (XRD), transmission electron microscopy (TEM), cathodoluminescence (CL) and other characterization techniques, we clearly evidenced that the formation of a Ruddlesden-Popper 'quasi-2D' perovskite phase through the surface coating strategy passivated the surface defects, changed the electronic structure at the surface of the 3D perovskite and resulted in better carrier lifetime and higher efficiency. Using the optimum 2D surface treatment condition to fabricate semi-transparent perovskite cells and measuring them in a four-terminal perovskite-silicon tandem configuration, we achieved a tandem efficiency of 27.7% with an interdigitated back-contact (IBC) silicon bottom cell and 26.2% with a passivated emitter with rear locally-diffused (PERL) silicon bottom cell in a 1 cm^2 size-matched tandem.

2. Results and Discussion

Figure 1 illustrates different 2D treatment strategies: surface coating and bulk incorporation. In the surface coating method, the 3D perovskite film is first spun on a substrate following a standard procedure and the substrate is subsequently annealed on a hot plate at 100°C for 30 minutes[15]. The quadruple-cation mixed-halide perovskite $Rb_{0.05}Cs_{0.095}MA_{0.1425}FA_{0.7125}PbI_2Br$ with a bandgap of 1.72 eV is utilized as the 3D perovskite framework. The 2D perovskite precursor (n-butylammonium bromide (BABr), iso-butylammonium bromide or t-butylammonium bromide diluted in 2-propanol with different concentrations) is then spun on top of the 3D perovskite film, followed by annealing at 100°C for 5 minutes. In the bulk incorporation method, different percentages of the 2D perovskite precursor (aliphatic alkylammonium cations in a mixture of dimethylformamide/dimethyl sulfoxide) are added into the 3D perovskite precursor to form a mixed 2D-3D perovskite precursor. The mixed solution is then spun on the substrates following the same procedure as mentioned above.

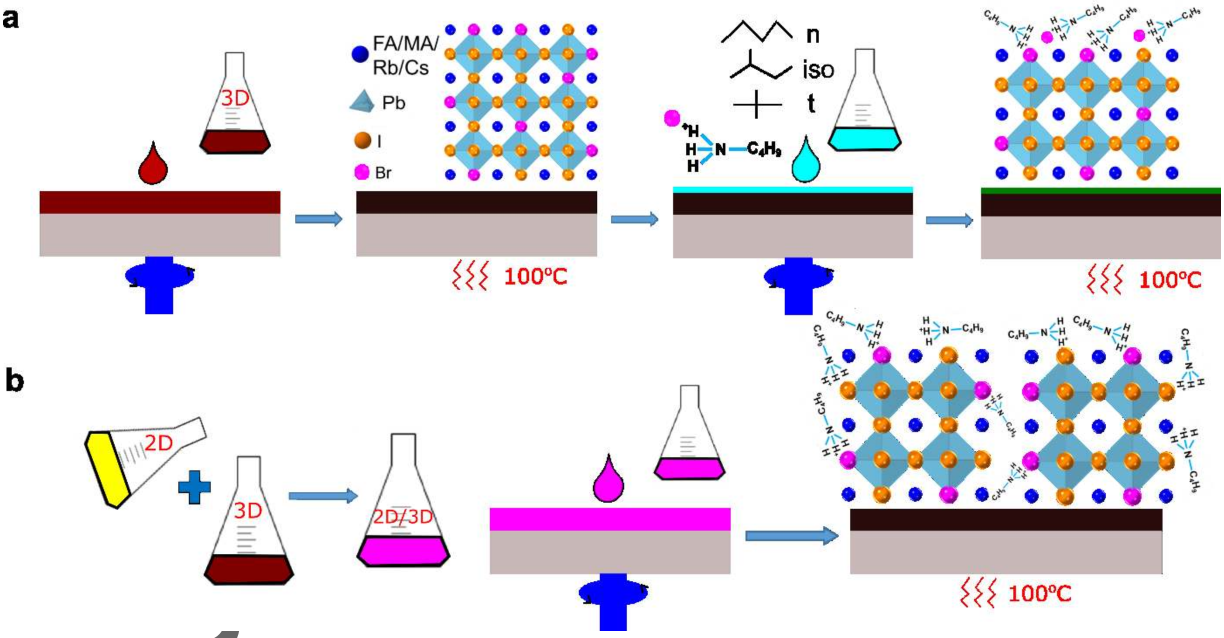

Figure 1. Schematic detailing two different 2D treatment routes for perovskite solar cell absorber layer. a – surface coating. b – bulk incorporation.

2.1. Photovoltaic Performance

We fabricated perovskite solar cells using perovskite active layers that underwent different 2D treatments as mentioned above in a n-i-p cell structure indium tin oxide / compact TiO_2 / mesoporous TiO_2 / perovskite / Spiro-MeOTAD / Au. Similar trends were observed in the device performance with surface coating and bulk incorporation, regardless of the choice of aliphatic alkylammonium bulky organic cations (**Figure S1, Table S1**). Thus, for the remainder of the work we only performed detailed investigations on the properties of samples treated with the n-butylammonium cation. Hereafter, we abbreviate the different 2D treatments as Surface - High: surface coating with high concentration (2.5 mg/ml), Surface - Low: surface coating with low concentration (1 mg/ml), Control: control sample, Bulk - Low: bulk incorporation with low concentration (2%) and Bulk - High: bulk incorporation with high concentration (5%). As shown in **Figure 2**, the control devices exhibited an average efficiency of 16.9% (reverse scan) with a respectable V_{OC} of 1.23 V. There was a small difference of ~3% between the efficiencies extracted from the reverse and the forward current density – voltage (*J*-*V*) scans. This hysteresis effect is well known in PSCs, which has been attributed to unbalanced charge carrier transport, ion migration, trap-assisted charge recombination and other possible causes[16]. With the low-concentration surface coating treatment, the efficiency was increased significantly by an absolute value of 1% to an average of 17.9%. In this condition, the champion device showed an efficiency of 18.3%. The efficiency enhancement came from a substantial increase in the V_{OC} to 1.26 V and noticeable increase in the fill factor (*FF*). In addition, the hysteresis in the devices was negligible. When the concentration of the 2D coating precursor was increased, the V_{OC} increased further to over 1.27 V, which is one of the highest values reported for perovskite solar cells with a similar bandgap (1.72 eV). However, the increase in the V_{OC} was compensated by a reduction in the FF and short circuit current density (J_{SC}). Thus, the average efficiency of PSCs using high concentration surface coating remained similar to the control devices. In contrast to the surface coating strategy, the devices using the bulk incorporation strategy showed dramatically reduced performance. The average efficiency was 14.9% with bulk incorporation - low concentration and was further reduced to 12.0% for the high concentration. The reduction in the cell performance was the result of drops in all the photovoltaic parameters. Moreover, the hysteresis became much more severe as indicated by a large difference in the efficiencies extracted from the *J-V* curves in both reverse and forward directions.

Given that the perovskite cell performance was improved with 2D surface coating, we further examined the impact of the surface coating on the stability of the devices. We tested the light stability of perovskite cells both with and without 2D surface coating. The devices were kept operating at a voltage close to the maximum power voltage under light and inside a custom-made sample holder with constant N2 flow, and *J-V* characteristics were determined every hour. Over 100 hours of operation, the control device retained about 88% of its initial efficiency, and the efficiency recovered to ~94% of its original value after two days in the dark (**Figure S2**). The device with surface coating showed slightly better light stability with the efficiency retaining about 93% of the initial efficiency after 100 hours and the efficiency recovered to over 99% of its original value after two days in the dark. As shown in **Figure S3** and **Figure S4**, we also detected reversible halide phase segregation in the control film and surface-coated film in agreement with previous work[17], however we have previously shown that, even though halide segregation occurs at the film level in both control and surface-passivated perovskite films, its impact at the device level is negligible when the perovskite solar cells operate under light near their maximum power point[18]. Therefore, the gradual drop in efficiency is likely to be due to the reversible migration of cations inside the active perovskite layer as reported previously[19], but further investigation is required to understand the exact degradation mechanism.

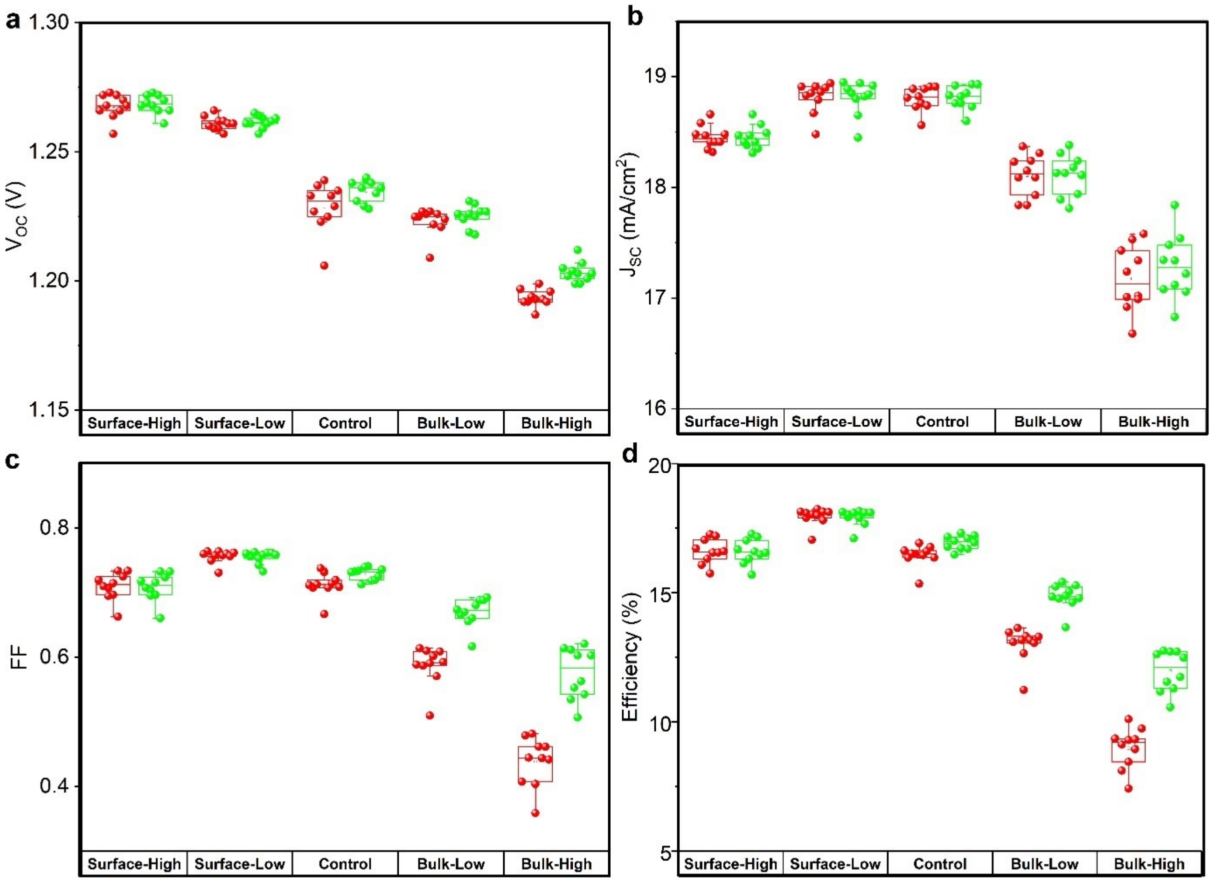

Figure 2. Distribution of photovoltaic parameters of perovskite solar cells with different 2D treatments extracted from *J*-*V* curves in both reverse (R, green) and forward (F, red) scanning directions. a – open circuit voltage (V_{OC}), b – short circuit current density (J_{SC}), c – fill factor (*FF*), d – efficiency. The scan rate is 50 mV/s in all the measurements.

2.2. Effect of Different 2D Treatments on the Surface Morphology, Crystal Structure, New Phase Formation and Lifetime of Perovskite Films

To understand the mechanisms behind the trend in photovoltaic performance of the devices when the perovskite films were subjected to the different 2D treatment routes, we first investigated the changes of the surface morphology and crystal size of the perovskite films. As shown in **Figure S5**, the control film exhibited crystal sizes ranging from 400 – 600 nm. The crystal sizes did not change in the case of surface coating with low concentration and no additional layer was observed on the film surface. When the concentration of the 2D surface coating precursor was increased, a thin layer on the surface could be seen although the grain sizes of the underlying 3D perovskite seem unchanged. This observation was verified by examining the cross-sectional SEM images of the samples. As shown in **Figure 3a-b**, both the control sample and the sample with surface coating – high concentration had monolithically grown grains with similar sizes extending throughout the thickness of the films. In addition, a very thin layer (~10 nm) was observed on top of the 3D perovskite film in the Surface – High film. In samples with bulk incorporation, the grain size becomes significantly smaller and ranges from 100 – 400 nm even with a concentration as low as 2%. The grain size also ranges from 100 – 400 nm when 5% of 2D perovskite was added into the 3D precursor. This resulted in the multiple grains stacking on each other throughout the thickness of the Bulk - High film as illustrated in **Figure 3c**. Reduction of perovskite crystal size upon precursor modification has also been observed previously e.g. when a large cation was incorporated into perovskite[10b, 20]. Interestingly, some features appeared on the films with brighter contrast suggesting the non-conducting nature of the features. The features not only appear in the bulk but also were detected on the surface of the sample. These results indicate that the presence of the 2D perovskite compound in the 3D perovskite precursor had a strong impact on the perovskite crystallization process. Since the BA cation has a too large effective radius to fit within the A sites of the perovskite structures i.e. the cages between the octahedral units, it could not be incorporated properly within the 3D perovskite structure. The bright features were indeed related to the formation of a pure 2D perovskite phase as evidenced by our results in the next sections. This indicates that the BA cation caused a distortion in the crystal structure and changed the crystallization kinetics of the perovskite[9, 21].

Next, we used time-of-flight secondary ion mass spectrometry (ToF-SIMS) to understand the distribution of different elements and species on the surface and interfaces of samples with different 2D treatments. **Figure 3d** shows the depth profile of Au^+ for the gold metal contact, CH_5O^+ for the

Spiro-MeOTAD, Pb^+ for the perovskite active layer, Ti^+ for the TiO_2, and Sn^+ for the transparent conducting oxide ITO, which thus represents the full device structure. The depth profile of the 2D n-butylammonium cation ($C_4H_{12}N^+$ with mass 74) is shown in **Figure 3e**, clearly showing the emergence of the 2D peak at the surface of the perovskite layer in the films with surface coating treatment. In the films with 2D perovskite incorporated in the bulk, the intensity of the 2D cation is slightly higher on the surface of the perovskite film and significantly higher near to the perovskite – TiO_2 interface. This phenomenon has previously been observed when incorporating $HOOC(CH_2)_4NH_3)_2PbI_4$ (AVAI) into the bulk of $MAPbI_3$ perovskite[22]. As shown in **Figure S6**, the roughness of the control perovskite film was 20.2 nm. With surface coating, the surface roughness was reduced to 14.9 nm and 10.3 nm with low concentration and high concentration, respectively. That indicates the 2D coating layer might fill the "valleys" and smooth out the surface of the underlying 3D perovskite layer. With the bulk incorporated samples, the roughness was also reduced significantly to 12.4 nm and 10.3 nm for low concentration and high concentration, respectively. This was mainly due to the smaller grain size of the perovskite crystals, in which the height difference between the grain interior and grain boundary was significantly reduced.

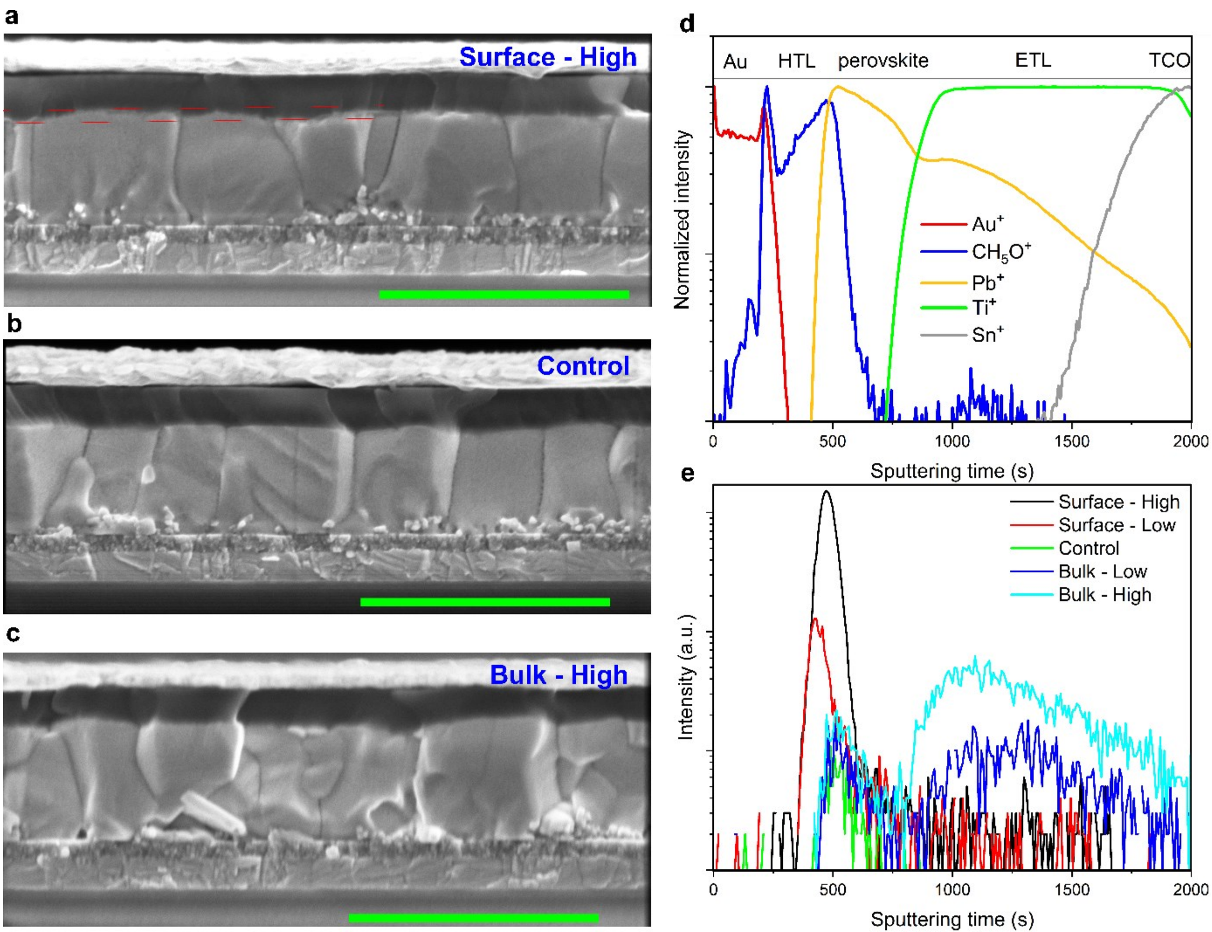

Figure 3. a– Cross-section of the perovskite cell with the perovskite film Surface - High (surface coating – high concentration). The red lines mark the presence of a thin layer on the surface of the 3D perovskite film. b - Cross-section of the perovskite cell with the control perovskite film. c - Cross-section of the perovskite cell with the perovskite film Bulk - High (bulk incorporation – high concentration). The scale bar is 1 µm. d – ToF-SIMS depth profiles of Au^+, CH_5O^+, Pb^+, Ti^+ and Sn^+ to show the complete structure of the device. e – ToF-SIMS depth profile of $C_4H_{12}N^+$ in perovskite films with different 2D treatments.

We checked the crystal properties of the perovskite films using X-ray diffraction (XRD). As shown in **Figure 4a**, the control film exhibited characteristic peaks at 14.4°, 20.4°, 25° and 28.9° which were indexed to (110)/(002), (112)/(200), (202) and (004)/(220) tetragonal phases, respectively. The main peak was located at 20.4° indicating that the perovskite film was oriented along the (112) and (200) directions. On the surface coated films, the dominant peak remained at 20.4° although the intensity of the peak was slightly decreased. Importantly, new peaks at 9.0° and 13.5° were detected and an additional peak at very low angle 4.5° could be found using grazing incidence XRD (**Figure S7**). These peaks did not correspond to the characteristic peaks of BABr located at 5.5° as reported previously[12]. Instead, these peaks were related to the Ruddlesden-Popper (RP) 'quasi-2D' perovskite $(BA)_2A_{n-1}Pb_n(I_xBr_{1-x})_{3n+1}$ with $n = 2$ as previously reported[23]. Here, A is the combination of small organic (FA, MA) and inorganic cations (Cs, Rb), where the exact composition remains unknown. In samples with bulk incorporation, a distinctively different peak positioned at 12.92° was detected in the bulk-incorporated samples with high concentration, which corresponds to the 2D perovskite $BA_2Pb(I_yBr_{1-y})_4$ phase. Interestingly, the main peak on the perovskite films changed to the position of 14.4°, which suggested that the films were oriented along the (110) and (002) orientation instead. This finding supports the hypothesis that the BA cation introduced in the 3D perovskite crystal causes the distortion in the crystal structure and changed the crystal orientation. Several reports indicate that the photovoltaic performance of perovskite solar cells depends on the crystal orientation of the perovskite crystals formed on the substrate[24]. However, it is still unclear which crystal orientation of the perovskite active layer would be more beneficial for the device performance since other factors such as device structure and the choice of charge transport layers need to be considered.

We used transmission electron microscopy (TEM) to confirm the formation of different phases in the perovskite films with different 2D treatments. **Figure 4b** shows the bright-field TEM image of a perovskite film with high concentration surface coating, in which a region with 2D perovskite on the surface can be seen (highlighted in yellow). From the high-resolution TEM (HRTEM) of this area (**Figure 4c-d**), it is evident that multiple phases with significantly different interplanar spacing are formed. One phase has an interplanar spacing of 3.62 Å, which matches with the (202) reflection of the 3D perovskite according to Bragg's law (**Table S2**). The other phase with much larger interplanar spacing (6.68 Å) is closely related to the 'quasi-2D' RP perovskite peak at 2θ = 13.5°. **Figures 4e-g** show the TEM and HRTEM of a perovskite film with 2D incorporated in the bulk at high concentration. In these images, the bright features identified in the SEM image can be observed and highlighted. The interplanar spacing calculated from the HRTEM image of the highlighted area is 6.81 Å, which can be assigned to the pure 2D perovskite phase peak at 2θ = 12.92°. The excellent agreement between the TEM and XRD results confirms the formation of the RP 2D perovskite phase $(BA)_2A_{n-1}Pb_n(I_xBr_{1-x})_{3n+1}$ (n=2) on the surface of the 3D perovskite when the bulky organic cation is used in the surface coating strategy, however the pure 2D perovskite phase is formed instead when the bulky organic cation is utilized in the bulk incorporation strategy.

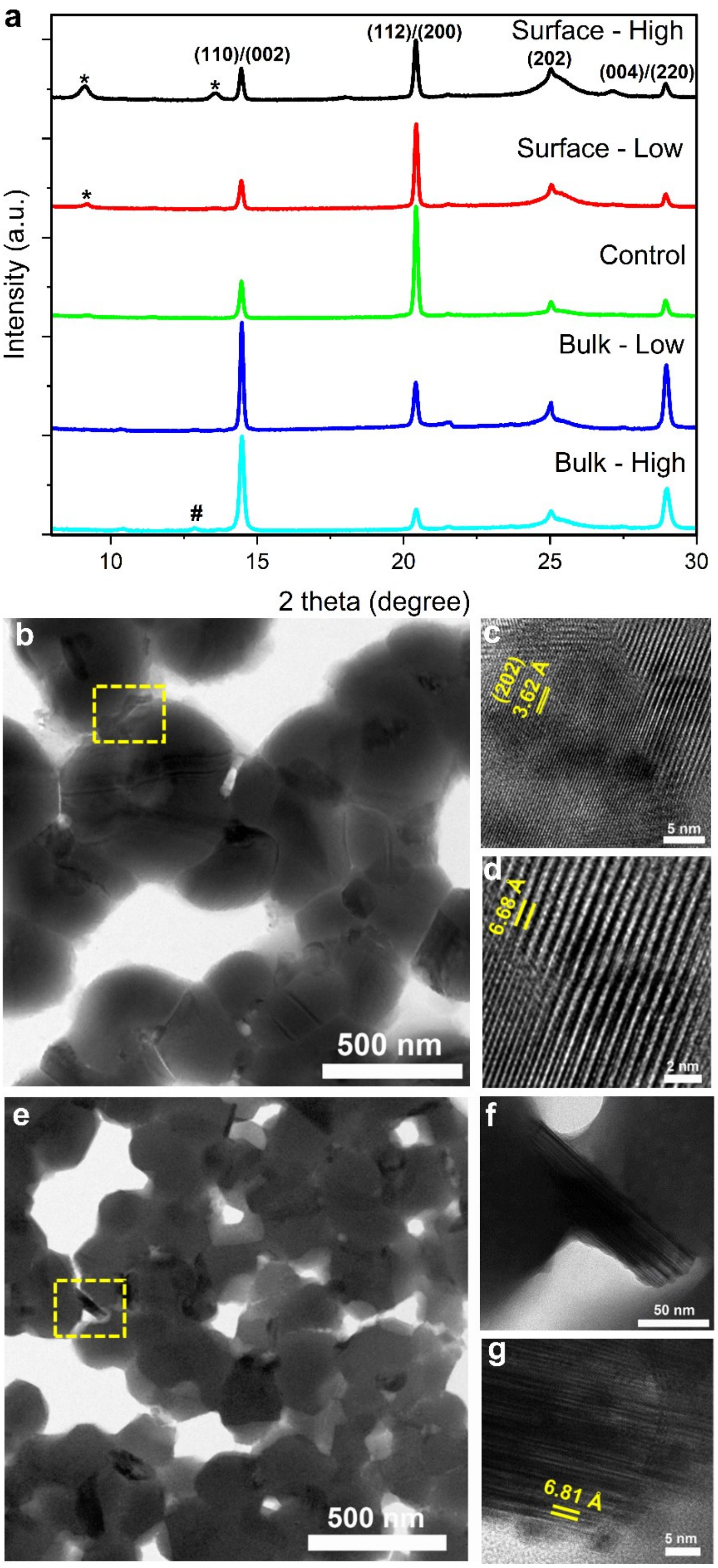
a
Intensity (a.u.)
2 theta (degree)
10
15
20
25
30
Surface - High
Surface - Low
Control
Bulk - Low
Bulk - High
(110)/(002)
(112)/(200)
(202)
(004)/(220)
*
*
*
#
b
500 nm
c
(202)
3.62 Å
5 nm
d
6.68 Å
2 nm
e
500 nm
f
50 nm
g
6.81 Å
5 nm

Figure 4. a – XRD patterns of perovskite films deposited on glass/ITO/ms-TiO_2 substrates with different 2D treatments. The * symbol represents the $(BA)_2A_{n-1}Pb_n(I_xBr_{1-x})_{3n+1}$ 2D perovskite phase and the # symbol represents the $BA_2Pb(I_yBr_{1-y})_4$ phase. b – bright-field TEM image of the perovskite films with surface coating - high concentration. c – HRTEM image of the highlighted region in b. d – Zoom-in of region highlighted in c to show the presence of the 'quasi-2D' RP perovskite. e - bright-field TEM image of the perovskite films with bulk incorporation – high concentration. f – HRTEM image of the highlighted region in e. g – Zoom-in of region highlighted in e to show the presence of the pure 2D phase.

To verify the findings, we used cathodoluminescence (CL) to characterize the different phases in perovskite films with the various 2D treatments[18, 25]. **Figure 5a,b** shows the magnified SEM images of the perovskite films with surface coating – high concentration and bulk incorporation – high concentration treatments. A thin layer of the 2D perovskite film can be observed on the surface of the 3D perovskite film on the Surface – High film, while some bright features can be clearly seen on the Bulk – High film. **Figure 5c** presents the CL spectra of the control film, the Surface-High film and the Bulk-High film (inside and outside of the bright features as marked in **Figure 5b**). The CL spectrum of the control film has a peak at ~ 720 nm, which agrees with the optical bandgap extracted from the absorption data. On the sample with surface coating at high concentration, we detected a CL spectrum with double peaks located at 720 nm and 610 nm. The latter corresponds to the emission peak of the thin Ruddlesden-Popper 2D perovskite film with n=2 reported in literature[23]. Interestingly, we detected a single peak CL spectrum at the area outside of the bright spot (Spot 1) and a double peak CL spectrum on the bright spot (Spot 2) of the bulk-incorporated sample. The additional peak of the CL spectra on the bright spot was positioned at the wavelength ~515 nm, which is close to the emission peak of the pure 2D perovskite (n=1). The photoluminescence spectra of the pure 2D perovskite (n=1), Ruddlesden-Popper 2D perovskite film (n=2) and 3D perovskite film are shown in **Figure S8**, which confirms the finding in the CL results. Furthermore, we applied two filters while capturing CL images, a 605 nm long pass filer to detect the main 3D perovskite peak and a 500±40 nm bandpass filer to detect the pure 2D perovskite $BA_2Pb(I_yBr_{1-y})_4$ peak. **Figures 5d** show a strong correlation of the bright features on the SEM image **(Figure 5b)** and the high luminescence areas on the bandpass filtered images. Those bright areas however appear dark on the long pass filter image (**Figure S9a**), which indicates lower luminescence at the wavelength of 720 nm. In the CL image of the Surface-High film with no filter (**Figure S9b**), the CL signal is relatively uniform which indicates that the 2D layer (n=2) is uniformly distributed through the surface of the 3D layer. We examined the absorbance spectra of perovskite films as shown in **Figure S10a**. The surface coated films exhibited similar absorbance spectrum to the control film. This indicated that a thin layer of the Ruddlesden-Popper 2D perovskite on the surface did not affect the absorption of the underlying 3D perovskite film. In contrast, a clear edge at ~500 nm could be observed in the bulk incorporated films with both low and high concentrations. In addition, the absorption coefficient was significantly lower in the case of bulk incorporated films as compared to the control film and surface-coated films (**Figure S11**). Although the bandgap as determined from the Tauc plot seemed unchanged at 1.72 eV for all the perovskite films **(Figure S10b)**, the emergence of the new absorbance edge at ~500 nm suggested that as the 2D was incorporated into the 3D perovskite precursor, a pure 2D phase was easily formed due to the chemical reaction of the BA cation with Pb and other halides (I, Br) and that this significantly changed the optical property of the films.

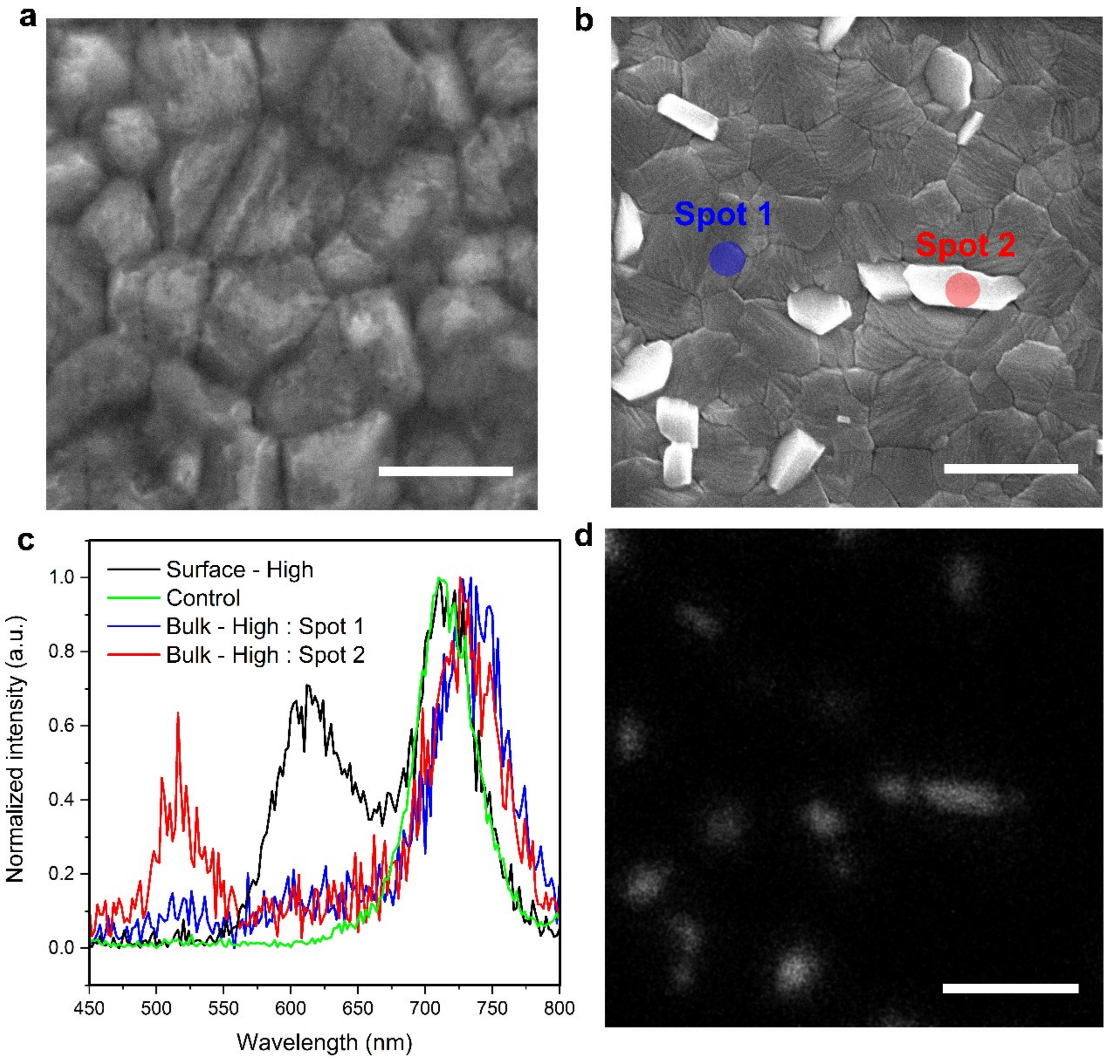

Figure 5. a - High magnification SEM picture of Surface – High film. b – High magnification SEM picture of Bulk – High clearly showing the bright spots. The scale bar is 500 nm. c – Cathodoluminescence spectra of perovskite Surface - High, Control and Bulk - High at two different spots. d – CL image of Bulk-High film using 500±40 nm bandpass filer. The penetration depth of the electrons in the CL measurement was calculated to range between 210 nm to 263 nm.

In order to evaluate how the changes in the film crystallinity and the formation of different phases affect the quality of the perovskite films, we applied thermally stimulated current (TSC) technique to probe the trap states in the device[26]. TSC was performed on full solar cells by filling the trap states using photo illumination at low temperature (18 K) and then devices were heated with a constant rate (7K/min) resulting in the release of trapped carriers. The current originating from the de-trapped carriers is measured as a function of temperature which gives the typical TSC spectrum. **Figure 6a** shows the TSC spectra of perovskite solar cells with different structures and with different 2D treatments. In the control device and device with low concentration surface coating, two distinct peaks were observed around 90 K (T1) and 235 K (T2) (red line). To identify the location of the traps, we performed TSC a on perovskite film without transport layers and only observed at peak at T2 in this sample (dark blue line). This indicated that the peak around T1 originated from one of the two transport layers while the peak around T2 came from the perovskite active layer. The magnitude of TSC peak at T2 in the surface coated device is found to be slightly lower than that of the control device. In the bulk incorporated device (cyan line), beside the common peaks at T1 and T2, an additional broad peak was observed at around 178 K (T3). Furthermore, the magnitude of TSC peak at T2 in the bulk incorporated device is higher than that of the control device. Due to the broadening of the TSC peaks, the average trap depth (Et) of the corresponding peak was estimated using[27]:

$$E_t = k_B T_m \ln({T_m}^4/b)$$

where is k_B is the Boltzmann constant, and T_m is the temperature of the TSC peak, and b is the heating rate. The current magnitude in the TSC signal is the measure of the number traps, and the lower limit of trap density was estimated from the time integral of TSC signal using:

$$\int I_{TSC} dt \le e N_t d A$$

where N_t is the trap density, e is the elementary charge, d is the thickness of the active layer and A is area of the device. The summary of trap depths and trap densities corresponding to each peak for all the devices is shown in **Table 1**. From TSC results, it can be concluded that the surface coating strategy reduced the number of traps while the bulk incorporation strategy increased the number of traps at the trap position E_t = 485 meV. The bulk incorporation strategy also created an additional trap level in the perovskite with a trap depth E_t = 350 meV and trap density $N_t = 1.25 \times 10^{16}$ cm^{-3}.

We used time resolved photoluminescence to measure the lifetime of the films. As shown in **Figure 6b** and summarized in **Table S3**, the lifetimes of the surface coated films with both low and high concentration were much higher than the control film. This indicates that formation of the Ruddlesden-Popper 2D perovskite on the surface of the 3D perovskite passivates the defects on the surface of the 3D perovskite. Surface defects have been regarded as the main source of non-radiative recombination in perovskite[28]. However, the reduction in the *FF* of the devices with surface coating at high concentration suggests that as the concentration of the surface coating precursor increased, the surface coating layer became excessively thick. Therefore, its insulating nature inhibited the carrier extraction in the device. In contrast, the life time of the bulk-incorporated film was much lower than the control films and the life time was further reduced with the higher concentration of the bulk incorporation. This agrees with the reduction in the crystal size, with more grain boundaries and the increase in the phase impurity (pure 2D phase $BA_2Pb(I_yBr_{1-y})_4$) acting as recombination centers inside the perovskite. In addition, since the structure of the pure 2D and its anisotropy induce an in-plane growth with layer orienting parallel to the substrate[6], it can hinder the charge transport from the bulk of the perovskite active layer to the charge transport layers. The transient PL results were also confirmed by measuring the steady state PL images of the devices under light and open circuit condition. As shown in **Figure 6c-e** and **Figure S12**, the devices with surface coating (both with low and high concentration) showed much higher PL counts than the control device, which was in line with the enhanced V_{OC} in the devices. This again emphasized the substantial reduction in the non-radiative recombination inside the device. In the case of bulk incorporation, especially the device with high concentration doping, the PL count was very non-uniform over the active area. Since the V_{OC} of the devices was much lower than the control device, the locally high PL count suggests misalignment of the energy levels between the perovskite and the electron and/or hole transport layers, which is further investigated in the next section.

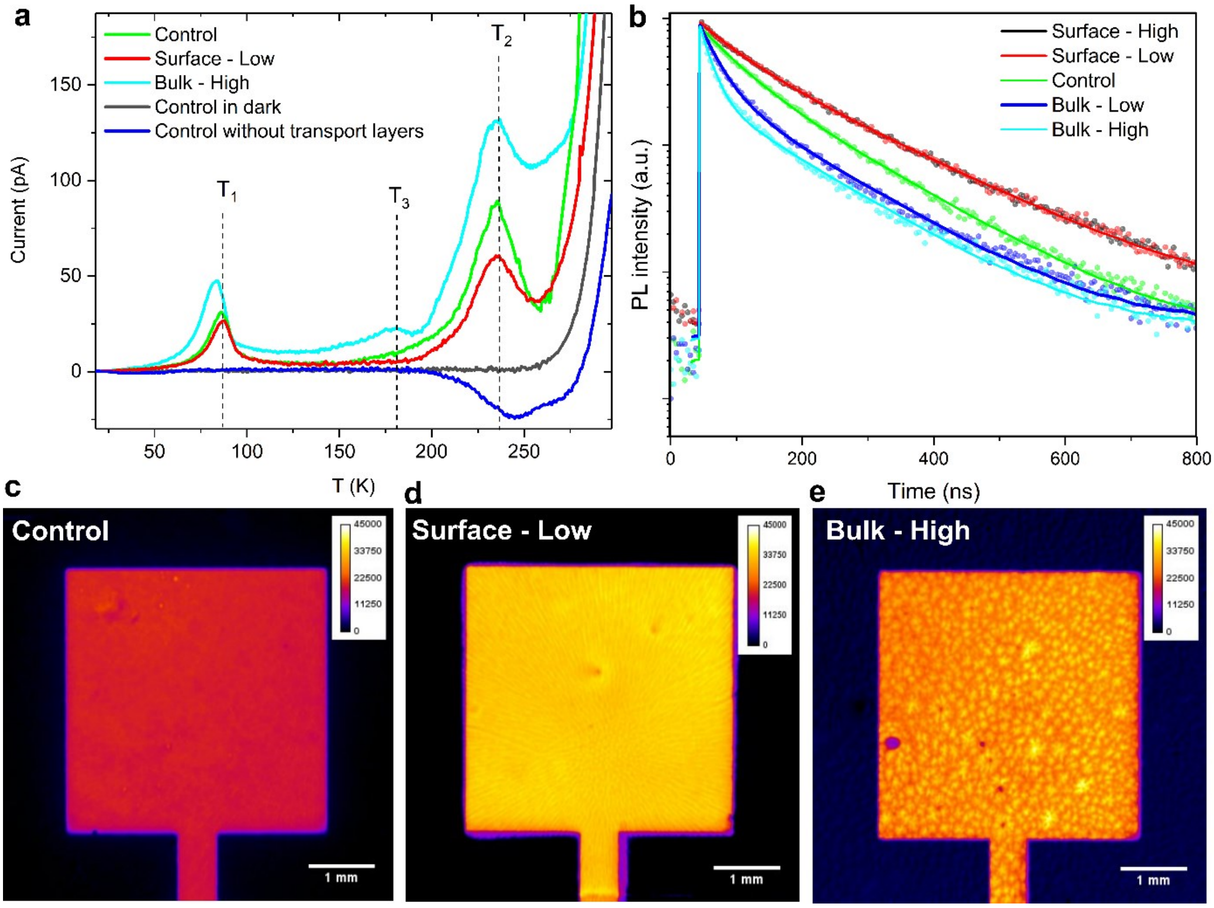

Figure 6. a – Thermally stimulted current (TSC) spectra of perovskite devices in different structure and with different 2D treatments. b - Time resolved photoluminescence of perovskite films with different 2D treatments. The fluence of the lase is ~10 μJ/cm^2/pulse. c – PL image of a control perovskite cell. d – PL image of a device with 2D surface coating – low concentration. e - PL image of a device with 2D incorporated in the bulk – high concentration.

Table 1. Calculation of the trap depth and trap density in perovskite device with different 2D treatments.

Device	Et_1 [meV]	Et_2 [meV]	Nt_1 [cm$^{-3]}$	Nt_2 [cm^{-3}]
Control	485	--	$3.12x10^{16}$	--
Surface - Low	485	--	$2.27x10^{16}$	--
Bulk - High	485	350	$5.68x10^{16}$	$1.25x10^{16}$

2.3. Impact on the Surface Chemistry and Electronic Structure of Perovskite Films

To understand the surface chemistry of perovskite films with different 2D treatments, we measured the x-ray photoelectron spectra (XPS) to quantitatively evaluate the change in the elemental composition at the surface of the films. In the C 1s spectra as shown in Figure 7a, three individual peaks positioned at 285.1 ± 0.15 eV, 286.8 ± 0.15 eV and 288.6± 0.15 eV were attributed to C-C, C-N and C=N bonding, respectively[29]. C-O could be excluded since no obvious oxygen signal was observed in the XPS data. From **Figure 7a**, it is evident that the C=N was decreased while the C-N was increased upon surface coating. In contrast, the relative concentration of different carbon species was relatively stable with the bulk incorporation. This finding was verified by fitting the N 1s spectrum as shown in **Figure 7b**, in which the peaks located at 400.9±0.15 eV (assigned to N=C) was decreased and the peak located at 402.5 ± 0.15 eV (assigned to N-C) was increased[30]. In addition, the C-C located at 285.6 ±0.15 eV for all the samples with 2D treatments, which is 0.5 eV higher than the control sample. A possible cause for this would be a dipole formed between the 2D perovskite material and the 3D material after the 2D treatments. Higher relative concentration of Br and lower relative concentration of I were also observed on the surface treated sample while these seemed unchanged with the bulk-incorporated samples (**Figure S13a-c**). The XPS results indicate significant change on the surface of the samples with 2D surface coating treatment, which supports the finding from the XRD that a thin Ruddlesden-Popper 2D perovskite film was formed on the surface of the 3D perovskite film. The less prominent change in the XPS in the samples with 2D incorporated in the bulk is understandable since the pure 2D phase $BA_2Pb(I_yBr_{1-y})_4$ is distributed throughout the bulk of the perovskite films and potentially near the perovskite/ETL interface. We also observed higher level of Pb defects in the samples with 2D incorporated in the bulk compared to the control sample and samples with surface coating by fitting the Pb 4f spectra (**Figure S13d,e**). We speculate that these Pb defects are under-coordinated Pb on the surface, which might lead to more surface recombination in the films[31].

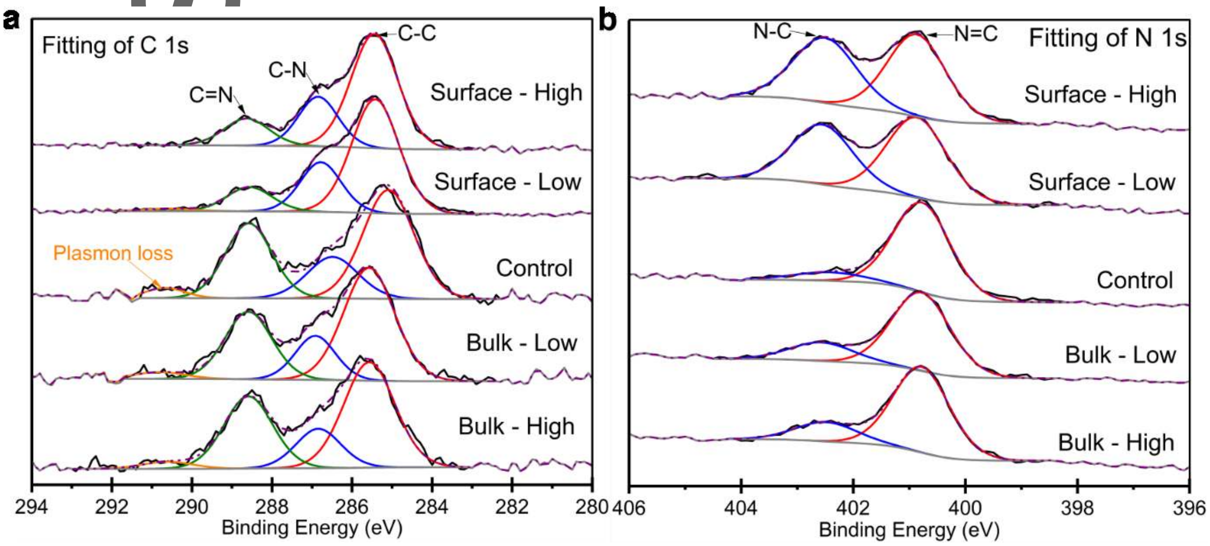

Figure 7. a – Fits of the high resolution XPS spectra of the C 1s of perovskite films with different 2D treatments. b – Fits of the N 1s spectra of the same set of samples.

To examine the electronic structure at the surface of perovskite films upon different 2D treatments, we used ultraviolet photoelectron spectroscopy (UPS) and inverse photoemission spectroscopy (IPES). **Figure 8a** illustrates the secondary electron cut-off region, the valence electron region of the UPS spectra and the conduction electron region of the IPES spectra for different perovskite films. The values for all the electronic levels and energies were extracted and are presented in **Figure 8b**. The control sample had a work function (*WF*) of 3.42 ±0.10 eV. The valence band was 1.3±0.10 eV below the Fermi level while the conduction band was 0.6±0.10 eV above the Fermi level, suggesting the n-type property of this perovskite semiconductor. An energy gap of 1.9±0.20 eV can be calculated from this data, which is substantially higher than the optical bandgap extracted from the absorption data (1.72 eV). This phenomenon has been observed previously (especially in organic semiconductors) and is well explained in a previous report[32]. In the samples with surface coating, the *WF* was significantly reduced to 3.37±0.10 eV and 3.17±0.10 eV for low and high concentration, respectively. In addition, the valence band was minimally shifted down to 1.35±0.10 eV below the Fermi level in both cases while the conduction band was also slightly shifted down to 0.45±0.10 eV for low concentration and 0.4±0.10 eV for high concentration above the Fermi level. The notable reduction in the *WF* of the materials suggests that the surface coating layer greatly modified the electronic properties of the 3D perovskite surface, such as energy level structure. Since Fermi level aligns due to the equilibrium of electrons at the perovskite/HTL interface[33], we speculate that this reduction in the *WF* of perovskite caused more upward energy band bending at the interface due to the increasing difference between the *WF*, and that this along with the reduction in surface defects was responsible for the enhanced V_{OC} and *FF* of the devices. In the bulk incorporated samples, the change in the *WF* was contrastingly different. The *WF* was increased to 3.62±0.10 eV and 3.92±0.10 eV for low and high concentration, respectively. In addition, the valence band was slightly shifted up to be 1.25±0.10 eV below the Fermi level for low concentration and seemed unchanged for high concentration. The conduction band, however, minimally shifted down to 0.5±0.10 eV above the Fermi level in both cases. The substantial increase in the *WF* of the perovskite might be responsible for the energy level misalignment between the perovskite/HTL interface, which resulted in much poorer device performance and the non-uniformity in the PL images described above.

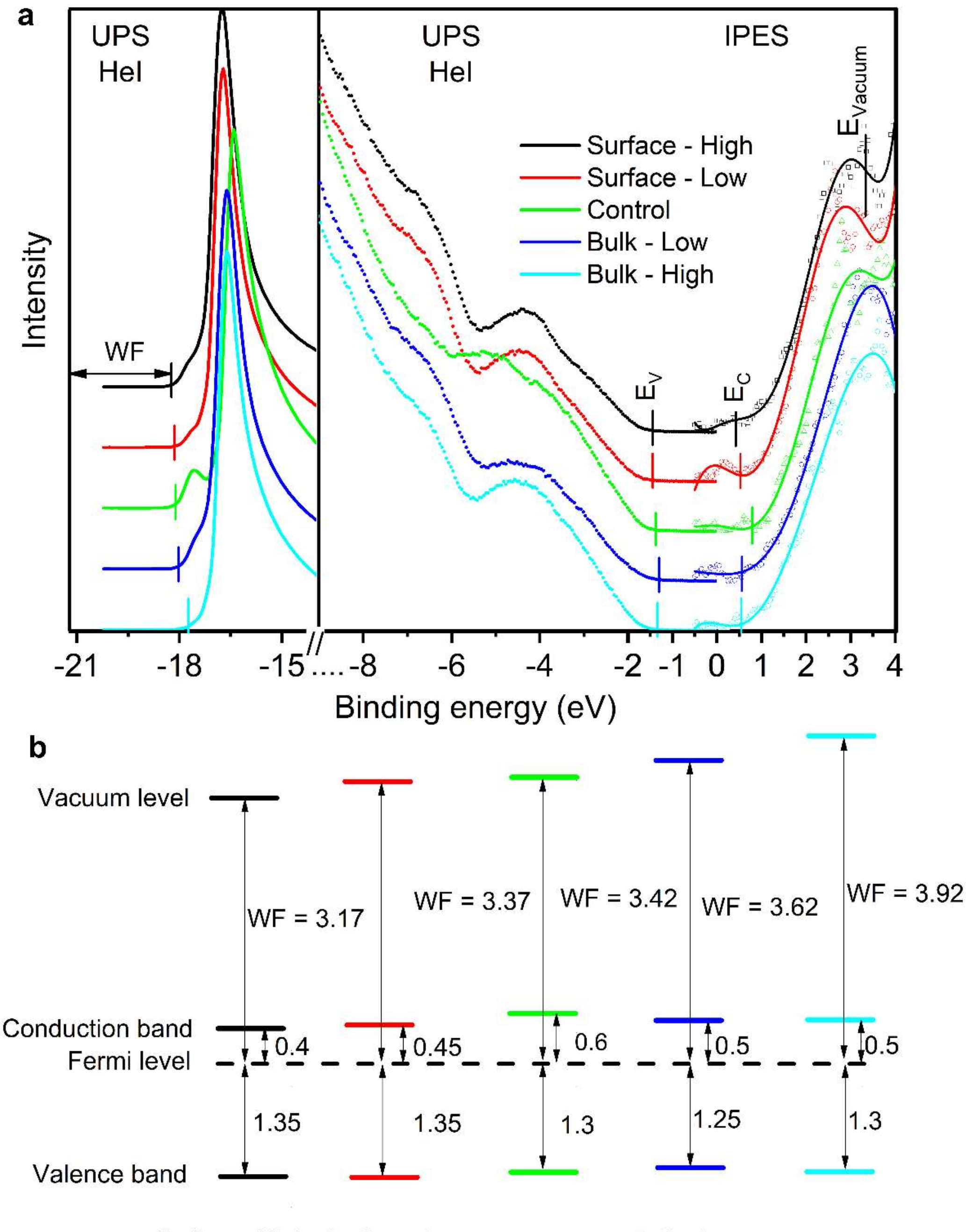

Figure 8. (a) UPS and IPES spectra of perovskite films with different 2D treatments. (b) Energy level diagram of perovskite films extracted from the UPS/IPES spectra. The uncertainty of the measured values is ±0.1 eV.

2.4. High Efficiency Four-terminal Perovskite-silicon Tandems

We previously reported an calculated efficiency of 26.4% when stacking a semi-transparent perovskite top cell, in which the opaque gold contact is replaced by a semi-transparent contact MoO_3/IZO, on top of a interdigitated back contact (IBC) silicon cells in a four-terminal tandem configuration[14]. To further improve the efficiency of the system, we need to improve the efficiency of each sub-cell and/or improve the optical management of the design[5]. Therefore, the enhancement in device performance resulting from the 2D surface coating with optimal concentration presented here should benefit the tandem efficiency. In addition, the application of the 2D surface coating layer reduces the surface roughness of the perovskite film. Therefore, we were able to reduce the thickness of the Spiro-MeOTAD layer to around 110 nm to reduce its parasitic absorption in the long wavelength region without affecting the cell reproducibility, which previously had been negatively affected[34]. We also thinned down the MoO_3 thickness from 10 nm to 5 nm to reduce the parasitic absorption of the layer as this layer becomes absorbing after the transparent conduction oxide sputtering process as shown in a previous report[35]. We used the surface coating – low concentration with n-butylammonium bromide to fabricate semi-transparent perovskite cells. The champion semi-transparent device exhibited an efficiency of 17.1% with negligible hysteresis and with the steady state efficiency of 17% after monitoring for 300 s (**Figure S14a**). The average efficiency of more than 20 fabricated devices was 16.5% (**Figure S15**) indicating good repeatability of the process. We note that lower value of V_{OC} was observed for semi-transparent devices since masking was applied during the measurement of these devices, which will lead to increased recombination in the shaded area. Without masking, the V_{OC} of semi-transparent devices is similar to the opaque devices (**Figure S16**). To minimize the reflectance loss in the four-terminal perovskite-silicon tandem solar cell, a textured foil was utilized on the top of the perovskite cell and a refractive index matching layer was applied between the perovskite and silicon cell (**Figure 9a**). The presence of the very thin 2D passivating layer negligibly impacted the transparency of the device. As shown in **Figure S17**, both the control device and device with surface coating absorb about 12-14% in the infrared region and they both had excellent transparency of over 80% in the long wavelength region. We prepared a 2.5 cm x 2.5 cm inactive perovskite device following a similar procedure as for the active devices. By stacking this on top of the interdigitated back contact (IBC) silicon cells[36], a silicon cell with an initial efficiency of 24.7% retained an efficiency of 10.7% under the perovskite filtered light (**Figure 9c**). Overall, we achieved a calculated efficiency of 27.7% (0.21 cm^2 semi-transparent perovskite cell and 4 cm^2 silicon cell) for the perovskite-silicon tandem in the four-terminal configuration. To our knowledge, this is the highest value reported for a four-terminal perovskite-silicon tandem. We carried out a light stability test of an encapsulated four-terminal perovskite-silicon tandem solar cell for 5 day/night cycles (12 hours under light and 12 hours in the dark for each cycle). The perovskite cell and silicon cell were held at fixed voltages close to their maximum power points and *J-V* curves were recorded every hour. We found that in each cycle, after 12 hours operating under light, the efficiency of the semi-transparent perovskite top cell retained around 95% of the initial efficiency recorded at the start of the cycle (**Figure S18**). The efficiency then recovered to about 98-99% of the efficiency recorded at the start of the previous cycle after the cell stayed in the dark for 12 hours. After five day/night cycles, the efficiency of the semi-transparent perovskite top cell retained 96% of the original efficiency. For the silicon bottom cell, the photocurrent was stable under light which indicated a negligible change in the absorption/transmission of the perovskite top cell (**Figure S19**). The overall four-terminal perovskite silicon tandem efficiency retained over 97% of the original efficiency after five day/night cycles (**Figure S20**). The result indicates that the four-terminal perovskite-silicon tandem solar cell is relatively stable under operating conditions, however more stability improvement is needed to achieve fully robust device.

Up-scaling of perovskite solar cells has been one of the major challenges in commercializing perovskite solar cells[37]. To show that the method of 2D surface coating could be applied for a larger area device, we fabricated semi-transparent cells (layout as in the inset of **Figure 9d**) with an active area of 1.21 cm^2 and measured the cells using an aperture area of 1 cm^2. We achieved a steady state efficiency of 16.1% for the semi-transparent perovskite (**Figure S14b**), which was slightly lower than the small device due to series resistance. We combined this perovskite top cell with a 1 cm^2 passivated emitter with rear locally diffused (PERL)[38] silicon cell in a four-terminal tandem configuration. The silicon cell with an initial efficiency of 22.4% retained an efficiency of 10.1% when operating under the perovskite top cell. The lower efficiency of the PERL silicon cell as compared to the IBC cell when operating under the perovskite was mainly due to the difference in the spectral response of the silicon cells at long wavelengths as shown in the external quantum efficiency (*EQE*) results (**Figure 9b**). Nevertheless, the overall efficiency of the 1 cm^2 perovskite-silicon tandem reached 26.2% efficiency, which was not far behind the calculated efficiency when combining the small perovskite cell and filtered large IBC silicon cell (**Table 2**). Future work in engineering the ETL/perovskite interface to further enhance the V_{OC}, replacing the absorbing Spiro-MeOTAD HTL by other materials such as CuSCN and completely removing the MoO_3 interlayer is expected to boost the four-terminal perovskite-silicon tandem efficiency to 30%.

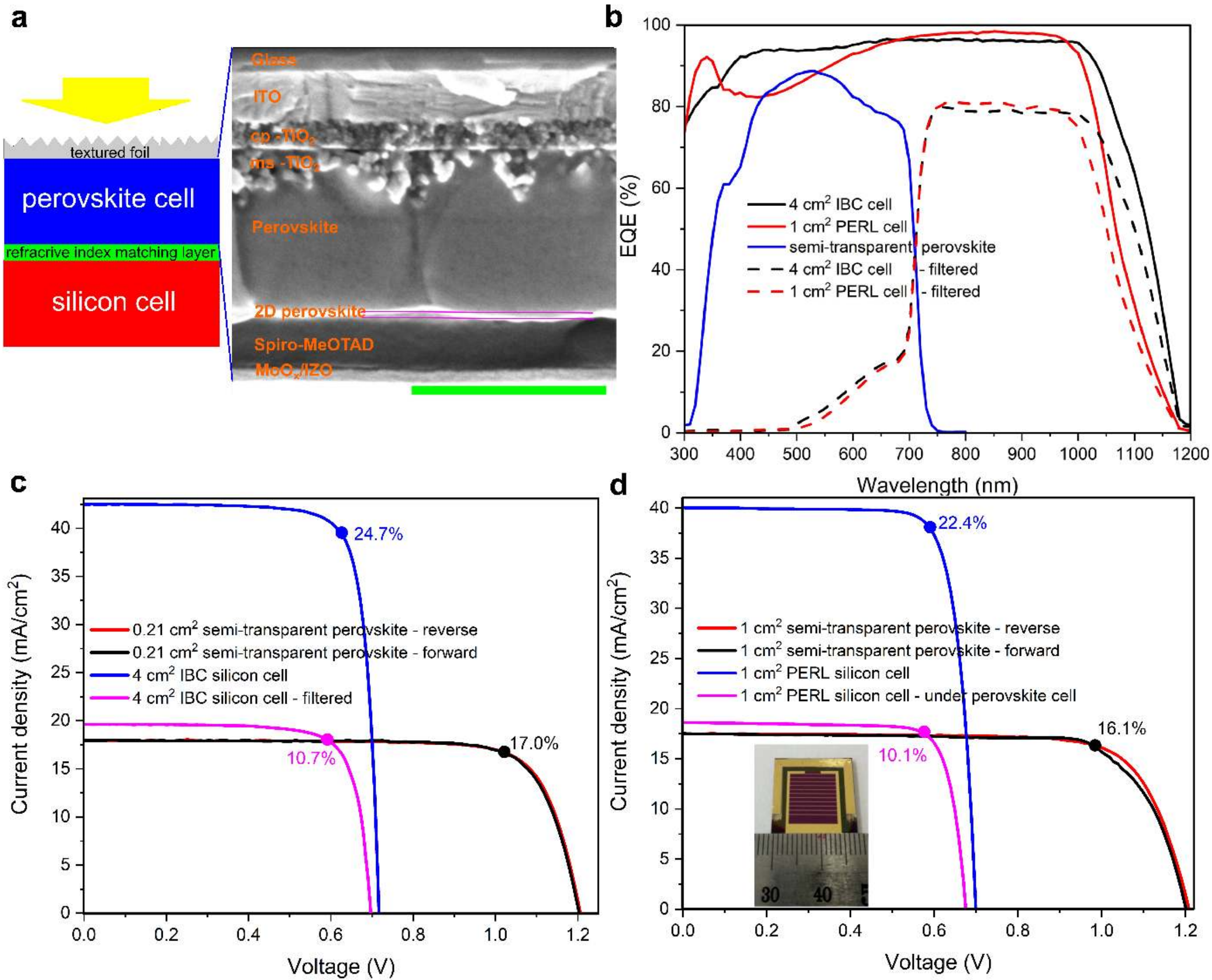

Figure 9. a – Schematic showing the four-terminal perovskite-silicon tandem in the four-terminal tandem configuration and the cross-section SEM image of a semi-transparent perovskite solar cell. The scale bar is 500 nm. b – *EQE* of perovskite cell and silicon cells performing as standalone devices or under the perovskite cell. c – *J-V* curves of perovskite-IBC silicon tandem. d – *J-V* curves of perovskite-PERL silicon tandem.

Table 2. Summary of the efficiency of perovskite – silicon tandems.

Devices	**Aperture [cm^2]**	**V_{oc} [V]**	**J_{sc} [mA/cm^2]**	***FF***	***Efficiency* [%]**
Semi-transparent perovskite cell	0.21	1.205	18.0	0.789	17.1

(reverse scan)					
Semi-transparent perovskite cell (forward scan)	0.21	1.202	18.0	0.785	17.0
Semi-transparent perovskite cell (steady state)	0.21				17.0
IBC silicon cell	4	0.717	42.5	0.81	24.7
IBC silicon cell (filtered)	4	0.697	19.6	0.78	10.7
Calculated four-terminal perovskite-IBC silicon tandem					**27.7**
Semi-transparent perovskite cell (reverse scan)	1	1.205	17.5	0.763	16.1
Semi-transparent perovskite cell (forward scan)	1	1.2	17.5	0.763	16.1
Semi-transparent perovskite cell (steady state)	1				16.1
PERL silicon cell	1	0.699	40.1	0.801	22.4
PERL silicon cell (under perovskite cell)	1	0.675	18.6	0.804	10.1
Four-terminal perovskite-PERL silicon tandem	1				**26.2**

3. Conclusion

In summary, we explored different strategies of combining 2D perovskite with 3D perovskite materials to further enhance solar cell performance. We found that by coating the surface of quadruple-cation mixed halide perovskite with different aliphatic alkylammonium bulky cations, the 2D Ruddlesden-Popper perovskite phase with *n*=2 was formed which passivated the surface defects, changed the electronic structure at the surface of the 3D perovskite and resulted in better carrier lifetime and higher efficiency. In contrast, incorporating the aliphatic alkylammonium bulky cations into the bulk of the 3D perovskite negatively affected the crystallinity, induced the formation of the pure 2D perovskite with *n*=1, greatly changed the electronic structure of the 3D perovskite and finally led to lower device performance. Using the surface coating strategy with n-butylammonium bromide cation, we fabricated semi-transparent perovskite cells with an efficiency up to 17.1% and average transparency over 80% in the long wavelength region. When combined with IBC silicon cells, we achieved an efficiency of 27.7% in a four-terminal perovskite-silicon tandem. In addition, a tandem efficiency of 26.2% was attained when combining 1 cm^2 semi-transparent perovskite cell with 1 cm^2 PERL silicon cell. The work paves the way for the development of high efficiency four-terminal perovskite-silicon tandems.

4. Experimental Section

4.1. Materials

Formamidinium iodide, formamidinium bromide, methylammonium iodide, methylammonium bromide, n-butylammonium bromide, iso-butylammonium bromide, t-butylammonium bromide, TiO_2 paste were ordered from GreatCell Solar Materials. Lead iodide was ordered from Alfa Aesar. Spiro-MeOTAD was ordered from Lum-Tech. Refractive index matching layer (series AA, refractive index = 1.414) was ordered from SPI Supplies. Other materials were ordered from Sigma Aldrich.

4.2. Solar Cell Fabrication

ITO glass substrates were cut into 1.45 cm * 1.25 cm and cleaned in ultrasonic bath with detergent for 90 minutes and for 15 minutes in acetone, 2-propanol and ethanol sequentially. The substrates were further cleaned using UV Ozone for 30 minutes before being immediately transferred to a N_2 purging glove box. 70 nm of compact TiO_2 was deposited on the substrates by spinning a solution of TTIP in 2-propanol at 5000 rpm for 15 s. The substrates were then annealed at 500 ^oC for 30 minutes in air. 100 nm of mesoporous TiO_2 was deposited on the substrates by spinning a solution of TiO_2

paste in ethanol at 5000 rpm for 15 s. The substrates were then annealed at 500 °C for 30 minutes in air. 3D perovskite precursor (1 ml) was prepared by mixing of $FAPbI_2Br$ (0.75 ml, 1.3 mol in N,N-Dimethylformamide (DMF) / Dimethyl sulfoxide (DMSO) 4:1 volume ratio), $MAPbI_2Br$ (0.15 ml, 1.3 mol in DMF/DMSO 4:1 volume ratio), $CsPbI_2Br$ (0.1 ml, 1.3 mol in DMSO) and RbI (0.05 ml, 1.3 mol in DMSO). Perovskite was deposited on the substrates by spinning the solution (40 µl) at 2000 rpm for 10 s (acceleration rate 200 rpm/s) and 6000 rpm (acceleration rate 1000 rpm/s) for 20 s. 5 s before the program ends, chlorobenzene (150 µl) was quickly dropped on the middle of the substrates. This was then followed by an annealing at 100°C on a hotplate for 30 minutes. For 2D surface coating, n-butylammonium bromide (90 µl) diluted in 2-propanol with different concentrations (1 mg/ml for low concentration, 2.5 mg/ml for high concentration) was spun on the substrates at 5000 rpm for 30 s. The substrates were further annealed at 100°C for 5 minutes. In case of iso-butylammonium bromide and t-butylammonium bromide, the optimal concentrations were found to be 1.6 mg/ml and 3 mg/ml, respectively. For 2D incorporation in the bulk, mixture of n-butylammonium iodide (0.87 mol), n-butylammonium bromide (0.43 mol), lead iodide (0.87 mol), and lead bromide (0.43 mol) in DMF/DMSO (1 ml, 4:1 volume ratio) was added into the 3D perovskite precursor with different ration (2% for low concentration and 5% for high concentration). The molar ratios were the same for other aliphatic alkylammonium bulky cations. The perovskite film was then deposited following the same procedure as described above. Spiro-MeOTAD layer was deposited on the perovskite films by spinning solution of Spiro-MeOTAD (40 µl, 72 mg/ml) in chlorobenzene with Li-TFSI (17.5 µl, 520 mg/ml in acetonitrile) and 4-tBp (28.5 µl) at 4000 rpm for 30 minutes. For opaque devices, 100 nm of Au was deposited on the substrates by thermal evaporation through a shadow mask with an active area of 0.16 cm^2. For semi-transparent devices, 5 nm of MoO_3 was deposited on the substrate by thermal evaporation at very low vacuum (2×E-7 Torr). 30 nm of IZO was then deposited on the substrates by radio frequency sputtering through a shadow mask with an active area of 0.36 cm^2. Metal grids were deposited on top of the IZO layers by E-Beam evaporation. For large area device, substrates with size of 1.8 cm * 1.8 cm were used instead and a shadow mask with an aperture of 1.44 cm^2 was used to define the active area. To integrate large area perovskite solar cell and silicon solar cell in an area-matched four-terminal tandem, the 1 cm^2 PERL silicon cell was directly placed underneath the semi-transparent perovskite top cell. A refractive index matching layer was put between the two cell and a textured foil was placed on top of the perovskite top cell. Each cell was measured independently under simulated AM1.5G light. Four-terminal perovskite-silicon tandem solar cells were encapsulated between two glass substrates using butyl rubber edge sealant inside a glove box. Butyl rubber edge sealant was laid around the edge of each glass substrate while the device was attached in the middle of the glass substrate. The whole stack was placed in a custom-built jig and put on a hot plate at 95 ^{o}C (**Figure S21**). The thermal insulator in the middle of the jig limited the temperature experienced by the cell to below 70 ^{o}C. The four screws on the jig were tightened to press the stack down and the jig was kept at 95 ^{o}C for 15 minutes before cooling down to room temperature.

4.3. Characterizations

The *J-V* characteristic of the opaque perovskite cells was measured using solar simulator model #WAVELABS SINUS-220 equipped with a potentiostat source AutolabPGSTAT302N. The light intensity was calibrated at one Sun (100 mW/cm^2, AM1.5G) using the certified FraunhoferCalLab reference cell. Semi-transparent perovskite cells were measured in ambient using the same solar simulator and potentiostat. An opaque mask with an aperture of 0.21 cm^2 was used during the measurements. For large area semi-transparent cell, an opaque mask with an aperture of 1 cm^2 was used. Unless stated otherwise, the scan rate is fixed at 50 mV/s with a voltage step of 10 mV and dwell time of 200 ms. IBC silicon cells were measured using the same solar simulator and potentiostat under a 2.5 cm × 2.5 cm perovskite filter and a mask with an aperture of 4 cm^2 was used. PERL silicon cells were measured using the same solar simulator and potentiostat under a large area semi-transparent perovskite cell and a mask with an aperture of 1 cm^2 was used. X-ray diffraction is performed with a D2 Phaser X-Ray Diffractometer with step size of 0.01^o and integration time of 1s per step. Grazing incidence XRD was measured with a high-resolution PANalytical X'Pert PRO MRD system with the step size of 0.005^o and the integration time of 1s per step. Reflection/Transmission was measured with a Lambda 1050 spectrophotometer (Perkin Elmer) in integrating sphere mode. Cathodoluminescence (CL) measurement was performed on an FEI Verios scanning electron microscope (SEM) equipped with a GatanMonoCL4 Elite with the procedure as previously reported[25a]. CL images were captured in panchromatic mode with appropriate dichroic filters. A long pass filter at 605 nm and band pass filter 500 ± 40 nm were used. SEM surface and cross-sectional images were taken using the same system. TEM analyses were performed using a JEOL 2100F instrument on perovskite films spun on the carbon side of the copper TEM grid. TSC measurements were conducted in a closed cycle He cryostat using helium gas as the heat transfer medium. The atmosphere of the sample chamber was replaced with helium gas to make it inert. The possible traps were filled by illuminating a white LED array on the devices through an optical window for 5 minutes. After switching off the illumination, the device was kept in the dark for another 5 minutes to allow for thermalization of the carriers. Then, the device was heated up to room temperature with a constant rate of 7K/min. The TSC signal was monitored using a sub-femtoamp source meter (Keithley-6430) during the heating. No external voltage was applied to measure the current and the built-in field was used to collect the de-trapped carriers. Steady state photoluminescence measurements were performed using a custom-made PL setup. A pulsed laser of 365 nm with a repetition rate of 1 kHz was used for the excitation of the samples, with a fluence of ~1 µJ/cm^2. The steady state photoluminescence was captured using an ACTON spectrometer and a CCD camera PIMAX512 at room temperature. Time-resolved photoluminescence decay measurements were performed using LabRAM HR Evolution system with a time-correlated single photon counting (TCSPC) system (DeltaPro-DD, Horiba). A 508 nm diode laser (DD-510L, Horiba) with pulse duration of 110ps, μJ/ fluence of ~10 cm^2/pulse, and a repetition rate of 312.5kHz was used for excitation. Photoluminescence images of perovskite solar cells were taken following the procedure reported in our previous work[39]. In short, the illumination is provided by Lumileds blue light LEDs with a peak wavelength of emission of 450 nm filtered through Semrock FF01-451 band pass filters (400– 500 nm). Images were captured using a Princeton Instruments Pixis 1024 camera with a Peltier-cooled (−70 °C) silicon CCD detector. ToF-SIMS was performed using a dual beam depth profiling with Cs^+ primary ions for the erosion (1 keV, 75 nA) and primary beam Bi_3^+ for the analysis (15 keV, 0.4 pA). XPS was conducted in an ultra-high vacuum apparatus from SPECS, which maintains a base pressure at low 10^{-10} mbar. The Mg Kα line (12 kV, 200 W) is used for the measurements [40] with an UHV non-monochromatic X-ray source. The angle between the X-ray source and the analyser is 54°. Survey scan at a pass energy of 40 eV was processed first. High-resolution scans at a pass energy of 10 eV were then recorded for Mo, O and C. UPS was applied to determine the occupied electron states of a sample surface [41] and the minimum energy required for an electron to escape the surface (secondary electron). In the measurement, electrons were emitted with a UV radiation of 21.218 eV excitation energy, and thus collected by detector. The UPS was operated with in-situ XPS to avoid any contamination during sample transfer. IPES was used in this work for determining the unoccupied electron states of a sample [42], which was based on electron in/photon out mechanism. In the experiment, a beam of electron with specified energy was directed onto a sample surface, entering the unoccupied states and releasing photon with corresponding energy. The photon was detected by ionizing gas phase of a mixed Ar/acetone inside a Geiger-Müller tube. As a function of the kinetic energy of the electrons, the emitted photons allowed comprising the IPES spectrum. By operating in-situ IPES after UPS, a complete energy band structure of the sample was acquired. For determining the *WF*, the secondary electron cut-off on the binding energy scale of the UPS spectra was analyzed. The *WF* was taken by calculating the difference between the excitation energy of UV-light, which was 21.22 eV used for UPS, and the peak cut-off along the base line of the spectra. The value of valence band was determined by approximating the base line and the onset of valence electron peak of UPS with a linear curve and determining their intersections[43]. The same procedure was applied for determining the value of conductive band upon the conduction electron peak of IPES. When quantifying the peaks of XPS spectra, the intensity of peaks of various elements were normalized with atomic sensitive factor (ASF)[44]. The stability of four-terminal perovskite silicon tandem solar cells was carried out under simulated AM1.5G light in ambient. Fans were used to limit the temperature experience by the device to below 32 °C.

Supporting Information

Supporting Information is available from the Wiley Online Library or from the author.

Acknowledgements

This work has been supported by the Australian Government through the Australian Renewable Energy Agency (ARENA). Responsibility for the views, information or advice expressed herein is not accepted by the Australian Government. Part of the experiment was performed at Australian National Fabrication Facility (ANFF) ACT Node. T. D acknowledges the financial support of a Postdoc Fellowship from the Australian Centre for Advanced Photovoltaics (ACAP). T. W. is the recipient of an Australian Research Council Future Fellowship (project number FT180100302) funded by the Australian Government. Further, the authors would like to gratefully acknowledge the financial support by the Helmholtz Association through the HYIG of U. W. P. (FKZ VH-NG-1148), the project PEROSEED (FKZ ZT-0024), the Helmholtz Energy Materials Foundry (HEMF), the Recruitment Initiative of B. S. R. as well as the Karlsruhe School of Optics & Photonics (KSOP).

Conflicts of Interest

The authors declare no conflict of interest.

Received: ((will be filled in by the editorial staff))
Revised: ((will be filled in by the editorial staff))
Published online: ((will be filled in by the editorial staff))

References

[1] A. Kojima, K. Teshima, Y. Shirai, T. Miyasaka, *J. Am. Chem. Soc.* **2009**, 131, 6050.

[2] a) NREL. Efficiency chart. , https://www.nrel.gov/pv/cell-efficiency.html, accessed: 11/04/2019, 2019; b) M. A. Green, A. Ho-Baillie, H. J. Snaith, *Nat. Photonics* **2014**, 8, 506.

[3] T. P. White, N. N. Lal, K. R. Catchpole, *IEEE J Photovol* **2014**, 4, 208.

[4] M. Jaysankar, B. A. L. Raul, J. Bastos, C. Burgess, C. Weijtens, M. Creatore, T. Aernouts, Y. Kuang, R. Gehlhaar, A. Hadipour, J. Poortmans, *ACS Energy Lett.* **2019**, 4, 259.

[5] D. A. Jacobs, M. Langenhorst, F. Sahli, B. S. Richards, T. P. White, C. Ballif, K. R. Catchpole, U. W. Paetzold, *J Phys Chem Lett.* **2019**, 10, 3159.

[6] C. C. Stoumpos, D. H. Cao, D. J. Clark, J. Young, J. M. Rondinelli, J. I. Jang, J. T. Hupp, M. G. Kanatzidis, *Chem. Mater.* **2016**, 28, 2852.

[7] G. Grancini, M. K. Nazeeruddin, *Nat. Rev. Mater.* **2019**, 4, 4.

[8] B. Saparov, D. B. Mitzi, *Chem. Rev.* **2016**, 116, 4558.

[9] Z. Wang, Q. Lin, F. P. Chmiel, N. Sakai, L. M. Herz, H. J. Snaith, *Nat. Energy* **2017**, 2, 17135.

[10] a) J.-W. Lee, Z. Dai, T.-H. Han, C. Choi, S.-Y. Chang, S.-J. Lee, N. De Marco, H. Zhao, P. Sun, Y. Huang, Y. Yang, *Nat. Commun.* **2018**, 9, 3021; b) D. S. Lee, J. S. Yun, J. Kim, A. M. Soufiani, S. Chen, Y. Cho, X. Deng, J. Seidel, S. Lim, S. Huang, A. W. Y. Ho-Baillie, *ACS Energy Lett.* **2018**, 3, 647.

[11] a) T. M. Koh, V. Shanmugam, X. Guo, S. S. Lim, O. Filonik, E. M. Herzig, P. Müller-Buschbaum, V. Swamy, S. T. Chien, S. G. Mhaisalkar, N. Mathews, *J. Mater. Chem. A* **2018**, 6, 2122; b) Y. Cho, A. M. Soufiani, J. S. Yun, J. Kim, D. S. Lee, J. Seidel, X. Deng, M. A. Green, S. Huang, A. W. Y. Ho-Baillie, *Adv. Energy Mater.* **2018**, 8, 1703392.

[12] S. Gharibzadeh, B. Abdollahi Nejand, M. Jakoby, T. Abzieher, D. Hauschild, S. Moghadamzadeh, J. A. Schwenzer, P. Brenner, R. Schmager, A. A. Haghighirad, L. Weinhardt, U. Lemmer, B. S. Richards, I. A. Howard, U. W. Paetzold, *Adv. Energy Mater.* **2019**, 9, 1803699.

[13] K. T. Cho, G. Grancini, Y. Lee, E. Oveisi, J. Ryu, O. Almora, M. Tschumi, P. A. Schouwink, G. Seo, S. Heo, J. Park, J. Jang, S. Paek, G. Garcia-Belmonte, M. K. Nazeeruddin, *Energy Environ. Sci.* **2018**, 11, 952.

[14] T. Duong, Y. Wu, H. Shen, J. Peng, X. Fu, D. Jacobs, E.-C. Wang, T. C. Kho, K. C. Fong, M. Stocks, E. Franklin, A. Blakers, N. Zin, K. McIntosh, W. Li, Y.-B. Cheng, T. P. White, K. Weber, K. Catchpole, *Adv. Energy Mater.* **2017**, 7, 1700228.

[15] N. J. Jeon, J. H. Noh, Y. C. Kim, W. S. Yang, S. Ryu, S. I. Seok, *Nat. Mater.* **2014**, 13, 897.

[16] P. Liu, W. Wang, S. Liu, H. Yang, Z. Shao, *Adv. Energy Mater.* **2019**, 9, 1803017.

[17] a) E. T. Hoke, D. J. Slotcavage, E. R. Dohner, A. R. Bowring, H. I. Karunadasa, M. D. McGehee, *Chem. Sci* **2015**, 6, 613; b) C. G. Bischak, C. L. Hetherington, H. Wu, S. Aloni, D. F. Ogletree, D. T. Limmer, N. S. Ginsberg, *Nano Lett.* **2017**, 17, 1028.

[18] T. Duong, H. K. Mulmudi, Y. Wu, X. Fu, H. Shen, J. Peng, N. Wu, H. T. Nguyen, D. Macdonald, M. Lockrey, T. P. White, K. Weber, K. Catchpole, *ACS Appl. Mater. Interfaces* **2017**, 9, 26859.

[19] K. Domanski, B. Roose, T. Matsui, M. Saliba, S.-H. Turren-Cruz, J.-P. Correa-Baena, C. R. Carmona, G. Richardson, J. M. Foster, F. De Angelis, J. M. Ball, A. Petrozza, N. Mine, M. K. Nazeeruddin, W. Tress, M. Grätzel, U. Steiner, A. Hagfeldt, A. Abate, *Energy Environ. Sci.* **2017**, 10, 604.

[20] J. Lu, L. Jiang, W. Li, F. Li, N. K. Pai, A. D. Scully, C.-M. Tsai, U. Bach, A. N. Simonov, Y.-B. Cheng, L. Spiccia, *Adv. Energy Mater.* **2017**, 7, 1700444.

[21] G. Kieslich, S. Sun, A. K. Cheetham, *Chem. Sci* **2014**, 5, 4712.

[22] G. Grancini, C. Roldán-Carmona, I. Zimmermann, E. Mosconi, X. Lee, D. Martineau, S. Narbey, F. Oswald, F. De Angelis, M. Graetzel, M. K. Nazeeruddin, *Nat. Commun.* **2017**, 8, 15684.

[23] J.-C. Blancon, H. Tsai, W. Nie, C. C. Stoumpos, L. Pedesseau, C. Katan, M. Kepenekian, C. M. M. Soe, K. Appavoo, M. Y. Sfeir, S. Tretiak, P. M. Ajayan, M. G. Kanatzidis, J. Even, J. J. Crochet, A. D. Mohite, *Science* **2017**, 355, 1288.

[24] a) S. Bae, J.-S. Park, I. K. Han, T. J. Shin, W. H. Jo, *Sol. Energy Mater. Sol. Cells* **2017**, 160, 77; b) P. Docampo, F. C. Hanusch, N. Giesbrecht, P. Angloher, A. Ivanova, T. Bein, **2014**, 2, 081508; c) Q. Liang, J. Liu, Z. Cheng, Y. Li, L. Chen, R. Zhang, J. Zhang, Y. Han, *J. Mater. Chem. A* **2016**, 4, 223; d) G. Niu, H. Yu, J. Li, D. Wang, L. Wang, *Nano Energy* **2016**, 27, 87.

[25] a) T. Duong, H. K. Mulmudi, H. Shen, Y. Wu, C. Barugkin, Y. O. Mayon, H. T. Nguyen, D. Macdonald, J. Peng, M. Lockrey, W. Li, Y.-B. Cheng, T. P. White, K. Weber, K. Catchpole, *Nano Energy* **2016**, 30, 330; b) W. Li, M. U. Rothmann, A. Liu, Z. Wang, Y. Zhang, A. R. Pascoe, J. Lu, L. Jiang, Y. Chen, F. Huang, Y. Peng, Q. Bao, J. Etheridge, U. Bach, Y.-B. Cheng, *Adv. Energy Mater.* **2017**, 7, 1700946.

[26] a) A. Baumann, S. Väth, P. Rieder, M. C. Heiber, K. Tvingstedt, V. Dyakonov, *J Phys Chem Lett.* **2015**, 6, 2350; b) Y. Hu, E. M. Hutter, P. Rieder, I. Grill, J. Hanisch, M. F. Aygüler, A. G. Hufnagel, M. Handloser, T. Bein, A. Hartschuh, K. Tvingstedt, V. Dyakonov, A. Baumann, T. J. Savenije, M. L. Petrus, P. Docampo, *Adv. Energy Mater.* **2018**, 8, 1703057.

[27] C. Qin, T. Matsushima, T. Fujihara, W. J. Potscavage Jr., C. Adachi, *Adv. Energy Mater.* **2016**, 28, 466.

[28] B. Wu, H. T. Nguyen, Z. Ku, G. Han, D. Giovanni, N. Mathews, H. J. Fan, T. C. Sum, *Adv. Energy Mater.* **2016**, 6, 1600551.

[29] a) J. Díaz, G. Paolicelli, S. Ferrer, F. Comin, *Phys. Rev. B* **1996**, 54, 8064; b) L. G. P'yanova, V. A. Drozdov, A. V. Sedanova, N. V. Kornienko, *Russ. J. Appl. Chem.* **2019**, 92, 940.

[30] N. Hellgren, R. T. Haasch, S. Schmidt, L. Hultman, I. Petrov, *Carbon* **2016**, 108, 242.

[31] B. Chen, P. N. Rudd, S. Yang, Y. Yuan, J. Huang, *Chem. Soc. Rev.* **2019**, 48, 3842.

[32] J.-L. Bredas, *Mater. Horiz.* **2014**, 1, 17.

[33] Y. Yin, A. Sibley, J. S. Quinton, D. A. Lewis, G. G. Andersson, *Adv. Funct. Mater.* **2018**, 28.

[34] a) N. Marinova, W. Tress, R. Humphry-Baker, M. I. Dar, V. Bojinov, S. M. Zakeeruddin, M. K. Nazeeruddin, M. Grätzel, *ACS Nano* **2015**, 9, 4200; b) G.-W. Kim, D. V. Shinde, T. Park, *RSC Adv.* **2015**, 5, 99356.

[35] J. Werner, J. Geissbühler, A. Dabirian, S. Nicolay, M. Morales-Masis, S. D. Wolf, B. Niesen, C. Ballif, *ACS Appl. Mater. Interfaces* **2016**, 8, 17260.

[36] a) E. Franklin, K. Fong, K. McIntosh, A. Fell, A. Blakers, T. Kho, D. Walter, D. Wang, N. Zin, M. Stocks, E.-C. Wang, N. Grant, Y. Wan, Y. Yang, X. Zhang, Z. Feng, P. J. Verlinden, *Prog. Photovoltaics* **2016**, 24, 411; b) T. C. Kho, K. Fong, K. McIntosh, E. Franklin, N. Grant, M. Stocks, S. P. Phang, Y. Wan, E.-C. Wang, K. Vora, Z. Ngwe, A. Blakers, *Sol. Energy Mater. Sol. Cells* **2019**, 189, 245.

[37] Y. Rong, Y. Hu, A. Mei, H. Tan, M. I. Saidaminov, S. I. Seok, M. D. McGehee, E. H. Sargent, H. Han, *Science* **2018**, 361, eaat8235.

[38] D. Yan, S. P. Phang, Y. Wan, C. Samundsett, D. Macdonald, A. Cuevas, *Sol. Energy Mater. Sol. Cells* **2019**, 193, 80.

[39] D. Walter, Y. Wu, T. Duong, J. Peng, L. Jiang, K. C. Fong, K. Weber, *Adv. Energy Mater.* **2018**, 8, 1701522.

[40] a) K. Volgmann, F. Voigts, W. Maus-Friedrichs, *Surf. Sci.* **2012**, 606, 858; b) S. Oswald, *Surf. Interface Anal.* **2010**, 42, 1289.

[41] a) F. M. Spirkl, S. Kunz, F. F. Schweinberger, A. N. Farnbacher, R. Schroter, U. Heiz, *Rev Sci Instrum* **2012**, 83, 013114; b) K. Volgmann, F. Voigts, W. Maus-Friedrichs, *Surf. Sci.* **2012**, 606, 858.

[42] a) S. Park, J. Jeong, G. Hyun, M. Kim, H. Lee, Y. Yi, *Sci Rep* **2016**, 6, 35262; b) G. Krishnan, H. S. Al Qahtani, J. Li, Y. Yin, N. Eom, V. B. Golovko, G. F. Metha, G. G. Andersson, *J Phys Chem C* **2017**, 121, 28007.

[43] Y. Yin, D. A. Lewis, G. G. Andersson, *ACS Appl Mater Interfaces* **2018**, 10, 44163.

[44] C.D.Wagner, *J. Electron Spectrosc. Relat. Phenom.* **1983**, 32, 99.

Surface coating of 3D perovskite with alkylammonium bulky cations passivates the surface defects and improves the perovskite solar cell performance while incorporating those cations into the bulk negatively affects the crystallinity and reduces the device performance. Using the surface coating strategy, four-terminal perovskite-silicon tandem reaches an efficiency of 27.7% with interdigitated back-contact (IBC) silicon bottom cells.

Keyword: perovskite solar cell, wide bandgap, surface coating, perovskite-silicon tandem, 2-dimentional perovskite

The Duong*, Huyen Pham, Teng Choon Kho, Pheng Phang, Kean Chern Fong, Di Yan, Yanting Yin, Jun Peng, Md Arafat Mahmud, Saba Gharibzadeh, Bahram Abdollahi Nejand, Ihteaz M. Hossain, Motiur Rahman Khan, Naeimeh Mozaffari, YiLiang Wu, Heping Shen, Jianghui Zheng, Haoxin Mai, Wensheng Liang, Chris Samundsett, Matthew Stocks, Keith McIntosh, Gunther G. Andersson, Uli Lemmer, Bryce S. Richards, Ulrich W. Paetzold, Anita Ho-Ballie, Yun Liu, Daniel Macdonald, Andrew Blakers, Jennifer Wong-Leung, Thomas White, Klaus Weber, Kylie Catchpole*

Title: High Efficiency Perovskite-Silicon Tandem Solar Cells: Effect of Surface Coating versus Bulk Incorporation of 2D Perovskite

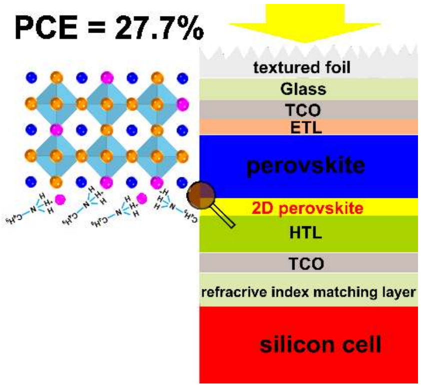

Author/s:

Duong, T;Pham, H;Kho, TC;Phang, P;Fong, KC;Yan, D;Yin, Y;Peng, J;Mahmud, MA;Gharibzadeh, S;Nejand, BA;Hossain, IM;Khan, MR;Mozaffari, N;Wu, YL;Shen, H;Zheng, J;Mai, H;Liang, W;Samundsett, C;Stocks, M;McIntosh, K;Andersson, GG;Lemmer, U;Richards, BS;Paetzold, UW;Ho-Ballie, A;Liu, Y;Macdonald, D;Blakers, A;Wong-Leung, J;White, T;Weber, K;Catchpole, K

Title:

High Efficiency Perovskite-Silicon Tandem Solar Cells: Effect of Surface Coating versus Bulk Incorporation of 2D Perovskite

Date:

2020-03-01

Citation:

Duong, T., Pham, H., Kho, T. C., Phang, P., Fong, K. C., Yan, D., Yin, Y., Peng, J., Mahmud, M. A., Gharibzadeh, S., Nejand, B. A., Hossain, I. M., Khan, M. R., Mozaffari, N., Wu, Y. L., Shen, H., Zheng, J., Mai, H., Liang, W. ,... Catchpole, K. (2020). High Efficiency Perovskite-Silicon Tandem Solar Cells: Effect of Surface Coating versus Bulk Incorporation of 2D Perovskite. Advanced Energy Materials, 10 (9), https://doi.org/10.1002/aenm.201903553.

Persistent Link:

http://hdl.handle.net/11343/275345